nature portfolio

https://doi.org/10.1038/s43017-021-00144-0

Supplementary information

Multifaceted characteristics of dryland aridity changes in a warming world

In the format provided by the authors and unedited

Multifaceted characteristics of dryland aridity changes in a warming world

Xu Lian, Shilong Piao, Anping Chen, Chris Huntingford, Bojie Fu, Laurent Z. X. Li, Jianping Huang, Justin Sheffield, Alexis M. Berg, Trevor F. Keenan, Tim R. McVicar, Yoshihide Wada, Xuhui Wang, Tao Wang, Yuting Yang, Michael L. Roderick

Appendix

Supplementary Methods

Precipitation and potential evapotranspiration (PET) data sets

To reduce uncertainties associated with the choice of precipitation and PET data sets, we used an ensemble of six gauge-based precipitation products, as well as six reanalysis-based products for PET, to estimate AI and its defined dryland extent. These precipitation diagnostic data sets were derived from the Climatic Research Unit (CRU)[1] TS4.0.1, the Climate Prediction Center (CPC)[2], the University of Delaware (UDel)[3], the Global Precipitation Climatology Project[4] (GPCP), the Global Precipitation Climatology Centre (GPCC) V4 (ref. 5), the Multi-Source Weighted-Ensemble Precipitation (MSWEP) V2.1 (ref. 6). The PET formulization involves climatic variables (air temperature, specific humidity, air pressure, wind speed and short- and long-wave radiation) obtained from reanalysis data sets of CRU-NCEP V8, Global Land Data Assimilation System[7] (GLDAS), NCEP/NCAR[8], Princeton Global Meteorological Forcing[9] (PGF), the second Modern-Era Retrospective analysis for Research and Applications[10] (MERRA-2), and the ECMWF ERA-Interim[11]. The lack of surface upward solar radiation (both short- and long-wave) in reanalysis outputs hinders the derivation of net radiation and thus PET. We thus used available outputs of sensible and latent heat fluxes, which can be added together to estimate surface net radiation, from two DGVMs (CABLE and ISAM, Table S2) driven by CRU-NCEP climatic forcings and observed atmospheric CO_2. All the climatic variables are available at monthly resolution but with varying spatial resolutions ($0.25^{o} \sim 1^{o}$), which were then resampled to a common $1^{o} \times 1^{o}$ resolution using a first order conservative remapping method. We derived an ensemble of AI estimates by considering all possible combinations of precipitation and PET data-based products. Some precipitation or PET products have limited temporal coverage, so we derived 16 ensemble members of AI for the longer 1948-2016 period, using four precipitation products (CRU, CPC, GPCC and Udel) and four PET products (CRU-NCEP, PGF, NCEP/NCAR and GLDAS). For

the shorter 1979-2016 period, we derived 36 members of AI since precipitation and PET are available in all databases. In addition, vapour-pressure deficit (VPD), which measures water demand of the near-surface air and is used in PET calculation (Eqn. 1), was calculated using the six reanalysis products and the ERA5 reanalysis[12].

Soil moisture and runoff data sets

Three observation-driven soil moisture data sets were used to quantify dryland soil moisture changes. These data include satellite-based soil moisture from the Global Land Evaporation Amsterdam Model (GLEAM v3.2a, root-zone soil moisture as a proxy for total soil moisture)[13] covering the period 1982-2016, the GLADS[7] covering 1948-2010, and the TerraClimate[14] covering 1958-2015. The three soil moisture products rely on different data assimilation systems and different climatic forcing inputs. To ensure comparability across different observation-driven data sets (and models), we transformed average total soil moisture (kg H_2O m^{-2}) of the study domain (**Fig. 1h**) to its fraction (%) of the simulated climatological mean during the baseline period 1961-1990, following previous studies[15].

We obtained runoff data of major river systems flowing through AI-defined dryland areas for the period 1948-2014, from the continental streamflow records of the world's large rivers database (http://www.cgd.ucar.edu/cas/catalog/surface/dai-runoff/index.html)[16,17]. We chose only river runoff data records that fulfil the following selection criteria: (1) less than 40% missing annual data during 1948-2014; (2) falls into the 100 largest rivers; and (3) at least half of the river basin area overlaps with AI-defined drylands. After applying these selection criteria, we identified a subset of 29 large rivers (listed in Table S4). For each of the 29 large river basins, we filled missing streamflow records during 1948-2016 with a linear interpolation based on catchment-mean precipitation records. In addition, we also obtained global gridded runoff maps from the Linear Optimal Runoff Aggregate (LORA) product, which used a bias-

correction and weighting approach to merge runoff estimates from hydrological models constrained by observed streamflow from a variety of sources[18]. This product is available at the monthly timescale and with a spatial resolution of 0.5° by 0.5°, for the period 1980–2012.

GIMMS NDVI 3g products

We employed the third-generation NDVI data (NDVI3g) generated by the Global Inventory Monitoring and Modeling Studies (GIMMS) group from the Advanced Very High Resolution Radiometer (AVHRR) sensors[19,20]. The GIMMS NDVI3g data set is available for the period of 1982-2016, with an 8 × 8 km spatial resolution and biweekly temporal resolution. We also obtained leaf area index (LAI) observations from the Moderate Resolution Imaging Spectroradiometer (MODIS, MCD15A2H) collection 6 product. This dataset provides LAI estimates at a spatial resolution of 500m and at every eight days, covering the period of 2000-2016. We composited the biweekly (or eight-day) values of NDVI (or LAI) to monthly using a maximum value approach. We only used NDVI (or LAI) values averaged over the growing season period to avoid spurious vegetation changes in the dormant season when the signal is flawed by the presence of snow cover. The start and end dates of the growing season were estimated from AVHRR-observed LAI dataset by a previous study[21].

Outputs of ESMs, DGVMs and GHMs

To examine the past and future aridity changes over drylands, we used diagnostic variables from 23 ESMs contributing to the CMIP5 archive under the "historical" (for the 1948-2005 period) and "RCP4.5" (for the 2006-2100 period) scenarios[22] (model details in Table S3). The RCP4.5 is an intermediate emission scenario and falls between a "a high-end emission" scenario (RCP8.5), and a massive reduction in emissions (RCP2.6) that might achieve global warming stabilization at 1.5 or 2.0°C above the pre-industrial level. For comparison, we also used 11 latest CMIP6 ESMs[23] under the

"historical" (for the 1948-2014 period) and "SSP2-RCP4.5" (for the 2015-2100 period, a scenario of intermediate emission and continuing historical socioeconomic activities) scenarios (model details in Table S6). All models selected provide sufficient diagnostics to calculate VPD, AI, soil moisture, runoff and GPP. This criterion filtered out AOGCMs that do not explicitly represent vegetation dynamics. We determined the timings of crossing the 1.5°C and 2°C global warming threshold above the pre-industrial level (as the 1850–1860 period) using time series of the global mean surface air temperature for each model. Note the time series were first smoothed with a 9-year running mean filter to reduce the impact of inter-annual variability of temperature, following previous studies[24,25]. In addition, following a similar method by Feng & Fu (2013) (ref. 26) (Eqn. 1), we adjusted the time-evolving AI derived from both CMIP5 and CMIP6 ESMs to have the same monthly climatology as observations (based on the average of 16 data combinations) during the same baseline period of 1961-1990.

$$\mathrm{AI}_{\mathrm{ESM\_adj},y} = \left(\mathrm{AI}_{\mathrm{ESM},y} - \mathrm{AI}_{\mathrm{ESM,1961\text{-}1990}}\right) + \mathrm{AI}_{\mathrm{obr,1961\text{-}1990}} \quad (1)$$

where $\mathrm{AI}_{\mathrm{ESM},y}$ and $\mathrm{AI}_{\mathrm{ESM\_adj},y}$ are the original and adjusted ESM estimates of AI for year y ($1948 \le y \le 2100$), respectively; and $\mathrm{AI}_{\mathrm{ESM,1961\text{-}1990}}$ and $\mathrm{AI}_{\mathrm{obr,1961\text{-}1990}}$ are the climatology of ESM-estimated and observation-based AI for 1961-1990, respectively. Such modifications better characterize the spatial extent of global drylands climatologically, while at the same time would not significantly influence the long-term changes of dryland extent (**Supplementary Fig. 7**).

We also used outputs from idealized CMIP5 ESM experiments forced by a 1% increase per year in atmospheric CO_2 concentration up to quadrupling the pre-industrial level over 140 years. We used the set of simulations (named ""esmFixClim1" in the CMIP5 terminology") in which the land surface component of the model responds to rising CO_2 but atmospheric component does not. This factorial simulation isolates physiological effects of rising CO_2 on terrestrial eco-hydrological changes, and associated feedbacks

on atmospheric conditions. We used seven ESMs including bcc-csm1-1, CanESM2, CESM1-BGC, GFDL-ESM2M, HadGEM2-ES, IPSL-CM5A-LR and NorESM1-ME, each with available outputs needed to calculate all aridity metrics.

We also used simulations of 12 offline DGVMs from the "Trends in net land-atmosphere carbon exchange" (TRENDY V6) project, for the period 1948-2016. Again, only models that have reported all the required variables for our analyses are used (details in Table S2). In the TRENDY project, input forcing data are prescribed for a series of factorial simulations for 1901-2016, following a standard experimental protocol[27]. The climatic forcings for the DGVMs were derived from the CRU-NCEP V8 (a merged product of monthly CRU observations and 6-hour NCEP reanalysis), and global annual atmospheric CO_2 data were from ice core and NOAA monitoring observations. We used two factorial simulations with varying prescribed forcings: (1) time-invariant climate and observed CO_2 (S1); and (2) transient climate and observed CO_2 (S2). Land use and land cover changes in both of those simulations are held unchanged. The individual effect of climate change was calculated directly from S1, and that of climate change is estimated as the difference between S2 and S1.

To assess changes of anthropogenic water stress, we also derived outputs of water availability and human water withdrawal from global hydrological models (GHMs) archived in the Inter-Sectoral Impact Model Intercomparison Project (ISIMIP 2b)[28], from the ESGF server (https://esg.pik-potsdam.de/search/isimip/). We only used GHMs with full outputs of surface runoff, and human water withdrawals by all the three sectors of agriculture, households, and industry, for both historical (1948-2005) and future periods (2006-2100). Only three GHMs (H08, MATSIRO and LPJml) that satisfy this criterion are available on the ESGF server in October 2020. These GHMs are driven by combinations of climate change scenarios (RCPs) and socio-economic development scenarios (SSPs). Climatic forcings for the GHM simulations are provided by four

CMIP5 ESMs including GFDL-ESM2M, HadGEM2-ES, IPSL-CM5A-LR and MIROC5. SSPs describe a range of plausible alternative socio-economic developments over the 21st century at the region level, including demographic, political, social, cultural, institutional, life-style, economic, and technological factors scenarios. As future impact projections under ISIMIP 2b didn't account for RCP4.5, here we included SSP2-RCP6.0 (a scenario of no-mitigation emission and continuing historical socioeconomic activities) for assessment. All the above model results were re-gridded to a common $1^{o}\times1^{o}$ grid before performing other analyses.

Quantifying dryland extent with different aridity metrics

Meteorological conditions shape the geographic distributions of soil moisture, runoff and vegetation cover at the land surface. We assumed that in present-day water-stressed regions, that is, drylands defined as regions with AI < 0.65, there also exists a permanent deficit of water in the ambient air (high VPD), soils (less soil moisture), rivers (less runoff), and for natural plants (low photosynthesis). We here characterized how these aridity metrics have changed in recent decades (1948-2016), and will change in the future (towards the end of the 21st Century), by performing the analyses described below.

We first established an empirical relationship between a given aridity metric (VPD, soil moisture, runoff and GPP) and AI using all grid points in the AI-defined drylands. This spatial relationship was built over the baseline period of 1961-1990 (or a subset of years thereof depending on data availability). Considering potential non-linearity in the system, we selected the empirical model, being either linear, polynomial and exponential, that can best describe the relationship between a given variable and AI (with the maximum R^2). With the pre-established regression models, we next determined the respective thresholds of VPD, soil moisture, runoff and GPP (or NDVI) for delineating dryland extent (**Supplementary Fig. 1**). We finally calculated year-to-

year variations of water-stressed areas (as a fraction of global land areas between -50°S~50°N) defined by VPD, soil moisture, runoff, and GPP, by applying the AI threshold of 0.65 to the temporally dynamic maps of these metrics respectively. These fractions, expressed as percentage changes relative to the baseline, are denoted by f_{AI}, f_{atm}, f_{soil}, f_{hyd}, f_{veg}, for AI, VPD, soil moisture, runoff and GPP, respectively, where a positive (negative) value implies an expansion (contraction) of water-stressed area compared to the baseline period of 1961-1990.

Supplementary Tables

Supplementary Table 1. A list of publications on dryland aridity changes grouped by different aridity metrics. We only include studies that characterise changes of the aridity level or areas of global drylands at the sub-continental or global scale.

Aridity type	Index	Domain	Data sources	Indicated changes	References
Atmospheric aridity	VPD	Global	Reanalysis output	Amplified increase of VPD compared with humid regions; No specific numbers reported.	Ref. 29
Surface aridity proxies	AI	Global drylands	Gauge-based precipitation and reanalysis-based PET	+4% for 1948-2015	Refs. 26,30,31
	AI	Global drylands	CMIP5 ESMs	+4-10% by 2100, based on original model results; +11-23% by 2100, based on bias-corrected model results	Refs. 30,32-36
	P-ET	Global arid and transitional regions	Observation-based data	10.8% of global land area show a robust 'dry gets drier, wet gets wetter' pattern for 1948-2005	Refs. 37,38
Hydrological aridity	Runoff	Australia	Gauge-based streamflow records	-24 to -28% for 1982–2010	Ref. 39
Soil moisture aridity	Soil moisture	Global drylands	Meta-analysis of field experiments	+17% with CO_2 enrichment	Ref. 40

	Water storage	Arid/semi-arid regions	Satellite data, hydrological modeling	-106.3 Gt water yr^{-1} for 1982–2010	Ref. 41
Soil moisture aridity	Soil moisture	Semi-arid grassland	Prairie Heating and CO_2 Enrichment (PHACE) experiment	+17% with 600 ppm ambient CO_2; -13% with +1.5/3.0 ºC day/night warming; non-significant increase with combined CO_2 enrichment and warming	Ref. 42
Ecological aridity	NDVI	Global semi-areas	Satellite data	+ 0.015 for 1981–2007	Ref. 43
	Foliage cover	Global arid regions	Satellite data	+5 to +10% for 1982–2010	Ref. 44
	L-band VOD	African drylands	Satellite data	-0.05 PgC yr^{-1} for 2010–2016	Ref. 45
	Above-ground biomass	Semi-arid grassland	Prairie Heating and CO_2 Enrichment (PHACE) experiment	+33% for warmed and CO_2-enriched plots	Ref. 42
	NDVI, L-band VOD	Global drylands	Satellite data	Greening in Sahel, India, western Australia, USA Great Plains; browning in eastern Australia, Mongolia; inconsistent trend elsewhere, for 1988-2008. No specific numbers reported.	Ref. 46

Supplementary Table 2. Details of the 12 TRENDY DGVMs used in this review.

Model name	Abbreviation	Spatial resolution
Community Atmosphere Biosphere Land Exchange	CABLE	0.5° × 0.5°
Community Land Model version 4.5	CLM4.5	1.25° × 0.9375°
Organizing Carbon and Hydrology in Dynamic Ecosystems	ORCHIDEE	0.5° × 0.5°
ORCHIDEE aMeliorated Interactions between Carbon and Temperature	ORCHIDEE-MICT	1° × 1°
Vegetation Integrative Simulator for Trace gases	VISIT	0.5° × 0.5°
Jena Scheme for Biosphere-Atmosphere Coupling in Hamburg	JSBACH	1.875° × 1.875°
Lund-Potsdam-Jena General Ecosystem Simulator	LPJ-GUESS	0.5° × 0.5°
Land Surface Processes and Exchanges model of the University of Bern	LPX-Bern	1° × 1°
Lund-Potsdam-Jena Wald Schnee und Landscaft version	LPJ-wsl	0.5° × 0.5°
The Joint UK Land Environment Simulator	JULES	1.875° × 1.25°
Integrated Science Assessment Model	ISAM	0.5° × 0.5°
Sheffield Dynamic Global Vegetation Model	SDGVM	1° × 1°

Supplementary Table 3. Details of the 23 CMIP5 ESMs used in this review.

Model name	Modeling center	Spatial resolution
CanESM2	Canadian Center for Climate Modeling and Analysis (CCCma), Canada	2.8125° × 2.8125°
GFDL-ESM2M	Geophysical Fluid Dynamics Laboratory, USA	2° × 2.5°
GFDL-ESM2G	Geophysical Fluid Dynamics Laboratory, USA	2° × 2.5°
IPSL-CM5A-LR	Institut Pierre Simon Laplace (IPSL), France	1.89° × 3.75°
IPSL-CM5A-MR	Institut Pierre Simon Laplace (IPSL), France	1.89° × 3.75°
IPSL-CM5B-LR	Institut Pierre Simon Laplace (IPSL), France	1.89° × 3.75°
GISS-E2-H	NASA Goddard Institute for Space Studies, USA	2° × 2.5°
GISS-E2-H-CC	NASA Goddard Institute for Space Studies, USA	2° × 2.5°
GISS-E2-R	NASA Goddard Institute for Space Studies, USA	2° × 2.5°
GISS-E2-R-CC	NASA Goddard Institute for Space Studies, USA	2° × 2.5°
NorthESM1-M	Norwegian Climate Center (NCC), Norway	1.875° × 3.25°
NorthESM1-ME	Norwegian Climate Center (NCC), Norway	1.875° × 3.25°
bcc-csm1-1	Beijing Climate Center, China Meteorological Administration, China	2.8125° × 2.8125°
bcc-csm1-1-m	Beijing Climate Center, China Meteorological Administration, China	2.8125° × 2.8125°
CESM1-BGC	National Center for Atmospheric	0.9° × 1.25°

	Research (NCAR), Boulder, USA	
CESM1-CAM5	National Center for Atmospheric Research (NCAR), Boulder, USA	0.9° × 1.25°
CCSM4	National Center for Atmospheric Research (NCAR), USA	0.9° × 1.25°
BNU-ESM	Beijing Normal University, China	2.8125° × 2.8125°
inmcm4	Institute for Numerical Mathematics (INM), Russia	1.5° × 2°
MPI-ESM-MR	Max Planck Institute for Meteorology (MPI-M), Germany	1.8758° × 1.8758°
MPI-ESM-LR	Max Planck Institute for Meteorology (MPI-M), Germany	1.8758° × 1.8758°
MIROC-ESM	National Institute for Environmental Studies, The University of Tokyo, Japan	2.8125° × 2.8125°
MIROC-ESM-CHEM	National Institute for Environmental Studies, The University of Tokyo, Japan	2.8125° × 2.8125°

Supplementary Table 4. Details of the 29 rivers flowing through global drylands (in descending order of basin area). We use continental streamflow records of world's large rivers to characterize dryland runoff changes[16]. Among the 921 world's biggest rivers, 29 rivers that meet the selection criteria described in Supplementary Methods were included in this study.

River name	Basin area (km^2)	Mouth location (latitude, longitude)	Annual mean discharge ($m^3 s^{-1}$) for 1961-1990	Linear trend of discharge ($m^3 s^{-1} yr^{-1}$) for 1948-2016
Murray	991000	24.25, 89.75	240.1	-2.22
Orange	850530	72.75, 126.75	189.6	-10.82
Huanghe	734146	-0.7500, -51.75	1264.8	-0.19
Rio	456700	48.75, -67.75	32.8	0.030
Colorado-AR	444701	9.250, -61.75	383.9	-3.35
Senegal	268000	-5.750, 12.75	731.3	-5.90
Fitzroy-QX	135860	29.75, -90.25	157.8	-0.57
Burdekin	129450	32.25, 120.75	263.4	-1.09
Liao	120764	-34.75, -57.75	81.3	0.29
Colorado-TX	108787	24.25, 88.25	68.8	-1.06
Guadiana	60883	70.75, 83.25	156	-0.55
Contas	56290	-2.250, -49.25	107	-0.88
Paraguacu	53866	9.750, 106.25	92.2	-1.15
Guadalquivir	46995	66.75, 69.25	124.5	2.74
Fitzroy-WX	46530	51.75, 140.25	208.6	-1.00
Luanhe	44100	10.75, -74.75	110.8	-0.07
Nueces	43149	4.750, 6.250	19.8	0.16
Tana	42217	68.75, -134.25	194.2	0.16
Colorado-SA	22300	46.25, -123.75	132.6	-0.07
Medjerda	20895	67.75, 53.25	20.4	-0.18
Blackwood	20400	48.75, -122.75	20.4	-0.14
Chubut	16400	-33.75, -58.25	46.9	-0.04
Jacuipe	10560	68.75, 160.75	11.6	0.04
Huasco	7187	-10.25, -36.75	5.6	-0.07

Doring	6903	24.75, 68.25	7.3	-0.11
Gongogi	6570	45.25, 28.75	38.3	-0.10
Mitta	4716	62.75, -164.25	33.7	0.05
Kiewa	1145	57.25, -92.75	16.6	-0.02
Big	356	64.75, 40.25	6.8	-2.22

Supplementary Table 5. Details of the 11 CMIP6 ESMs used in this review. All these ESMs selected provide sufficient diagnostics to calculate VPD, AI, soil moisture, runoff and GPP, for both the historical (1948-2014) and the near future (2015-2100).

Model name	Modeling center	Spatial resolution
ACCESS-ESM1-5	Commonwealth Scientific and Industrial Research Organization and Bureau of Meteorology, Australia	1.2414° × 1.8750°
CESM2-WACCM	National Center for Atmospheric Research (NCAR), Boulder, USA	0.94° ×1.25°
CanESM5	Canadian Center for Climate Modeling and Analysis (CCCma), Canada	2.8125° × 2.8125°
EC-Earth3-Veg	EC-Earth-Consortium	0.70° ×0.70°
INM-CM4-8	Institute for Numerical Mathematics (INM), Russia	1.5° ×2.0°
INM-CM5-0	Institute for Numerical Mathematics (INM), Russia	1.5° ×2.0°
IPSL-CM6A-LR	Institut Pierre Simon Laplace (IPSL), France	1.26° ×2.50°
MPI-ESM1-2-HR	Max Planck Institute for Meteorology (MPI-M), Germany	0.94° ×0.94°
MPI-ESM1-2-LR	Max Planck Institute for Meteorology (MPI-M), Germany	0.94° ×0.94°
NorESM2-LM	Norwegian Climate Center (NCC), Norway	1.875° ×2.5°
NorESM2-MM	Norwegian Climate Center (NCC), Norway	0.94° ×1.25°

Supplementary Figures

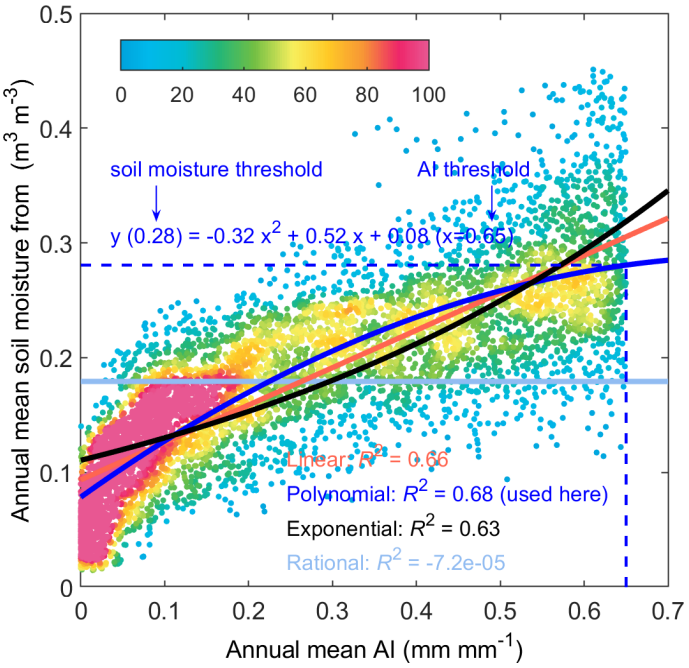

Supplementary Figure 1 | Determination of the threshold for water-stressed areas (soil moisture as an example). The established spatial relationship is between a specific aridity metric (VPD, soil moisture, runoff and GPP) and AI across geographical grid points distributed in drylands, for the baseline period of 1961-1990. Assuming that different aridity metrics generate similar dryland extents for the baseline period, we determine the threshold for each specific aridity metric using the established empirical relationship (either linear, exponential, quadratic or rational model) that yields the maximum R^2. The bold solid lines represent the best-fit regressions, and the dashed lines indicate the water-limitation thresholds of the aridity metrics (corresponding to AI = 0.65). The color bar in each panel indicate the density of grid points.

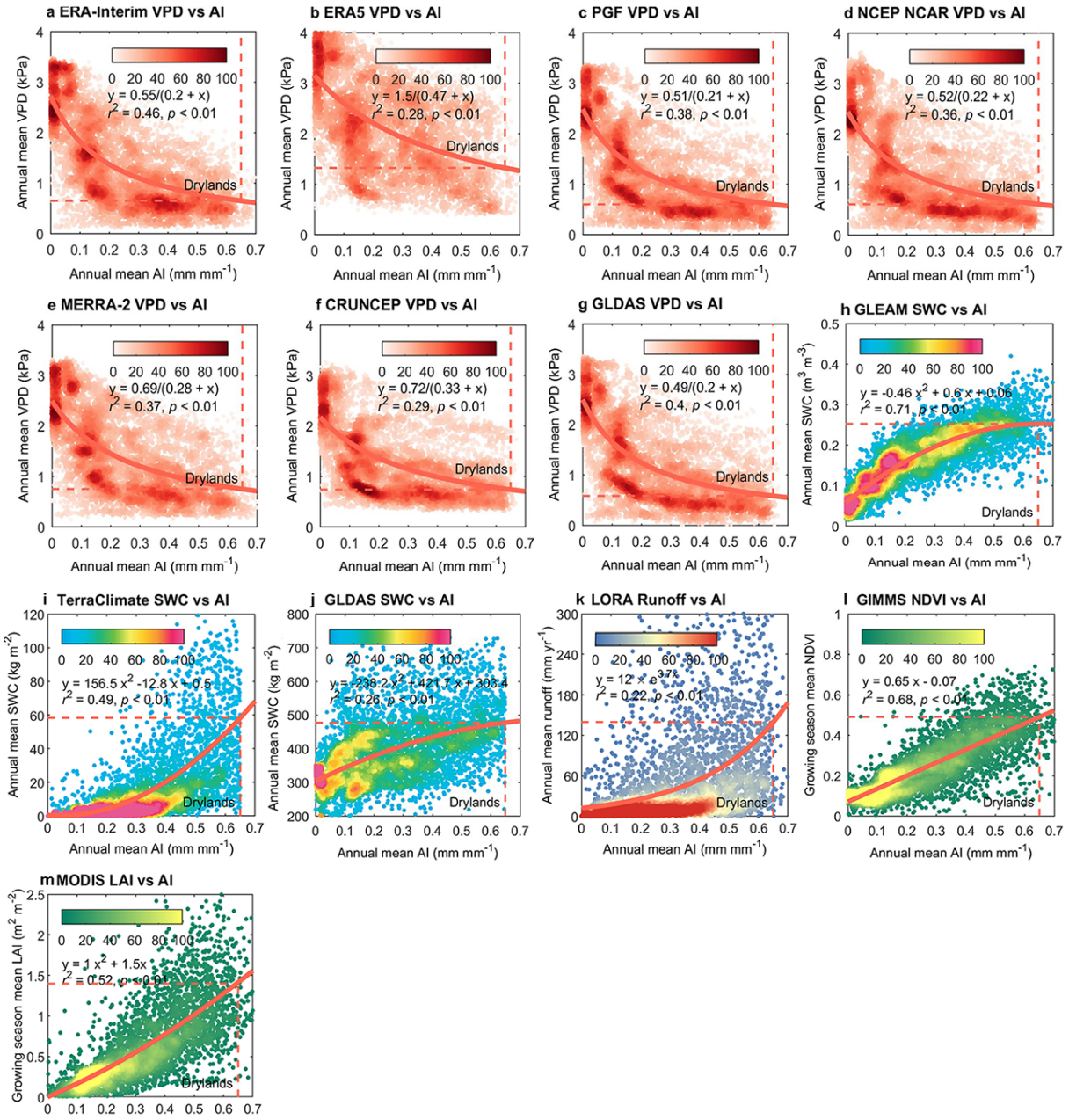

Supplementary Figure 2 | Observation-based relationship between AI and other aridity metrics. The best-fitted relationships between AI and other aridity metrics were established in a similar way as the example given in **Supplementary Figure 1**. Each panel shows the relationship between a specific aridity measure from different data sources and AI from an average of 16 precipitation and PET data combinations (see Supplementary Methods). SWC, VPD, NDVI and LAI denote soil water content, vapour-pressure deficit, normalized difference vegetation index and leaf area index, respectively.

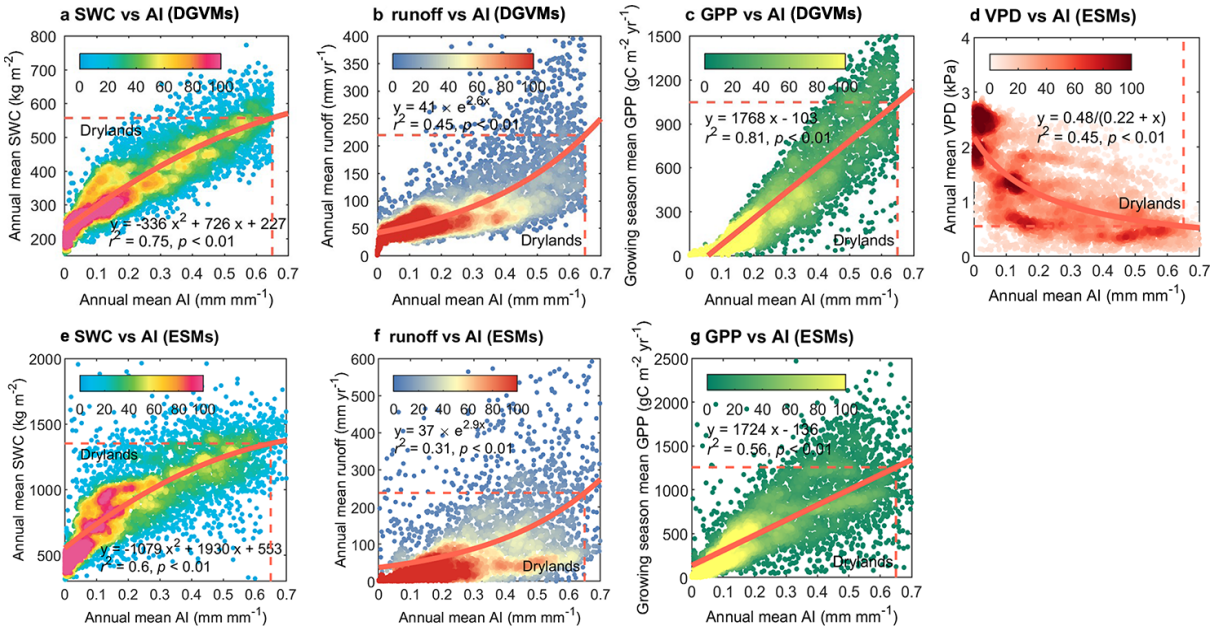

Supplementary Figure 3 | Model-based relationship between AI and other aridity metrics. The best-fitted relationships between AI and other aridity metrics were established in a similar way as the example given in **Supplementary Figure 1**. (**a-c**) use land surface variables from the TRENDY S2 simulation forced by elevated atmospheric CO_2 and climate change, and the AI is obtained from the CRU-NCEP data that provide climatic forcings for the TRENDY runs. (**d-g**) use land surface variables and AI from the CMIP5 historical simulation. Only relationships for the multi-model mean data are shown. SWC, VPD and GPP denote soil water content, vapour-pressure deficit and gross primary production, respectively.

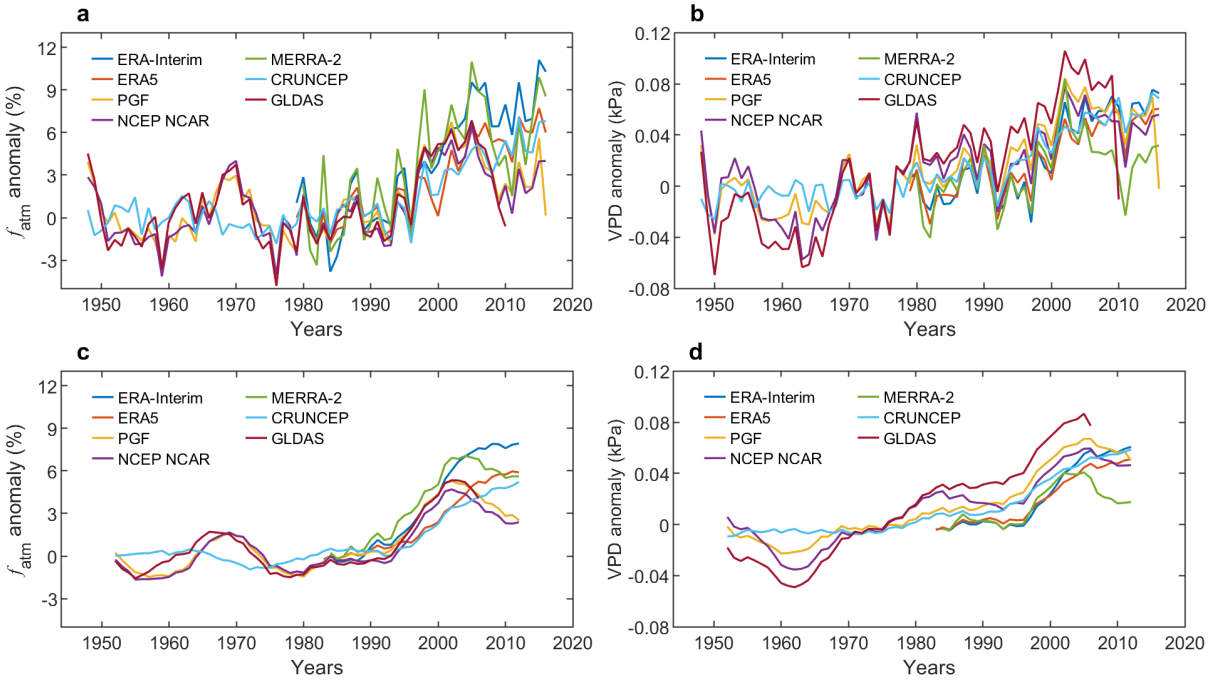

Supplementary Figure 4 | Anomalies of annual mean VPD (a) and its inferred f_{atm} changes (b) from various data sources. (**c**, **d**) | Similar as (**a**, **b**), except that all the times series are smoothed with a 9-year running mean filter for clarity. Anomalies are computed by subtracting the climatological mean of the 1961-1990 period (or a subset of years during this period depending on the temporal coverage of the input data). The annual mean VPD is averaged over the AI-defined drylands only.

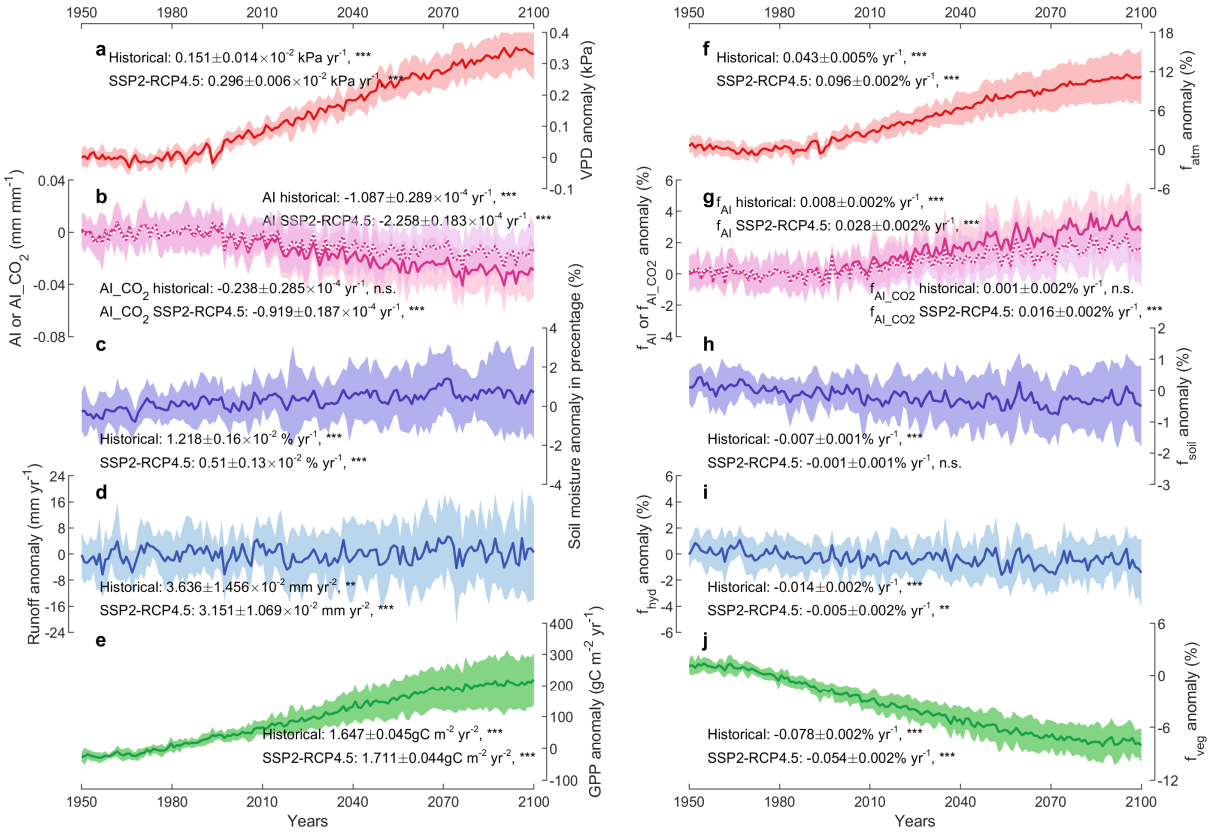

Supplementary Figure 5 | Dryland aridity changes evaluated with CMIP6 ESMs. a-e | Anomalies of VPD (**a**), AI (or AI_CO_2 that additionally accounts for CO_2 physiological impacts) (**b**), soil moisture (**c**), runoff (**d**) and GPP or NDVI (**e**), averaged over AI-defined baseline regions of drylands for 1961-1990. **f-j** | Anomalies of the fraction of water-stressed land areas (drylands) evaluated by VPD (f_{atm}) (**f**), AI (f_{AI}, or f_{AI_CO2} that additionally accounts for CO_2 physiological impacts) (**g**), soil moisture (f_{soil}) (**h**), runoff (f_{hyd}) (**i**) and growing-season mean GPP or NDVI (f_{veg}) (**j**) (details of the calculation of f_{atm}, f_{AI}, f_{AI_CO2}, f_{soil}, f_{hyd}, f_{veg} in Supplementary Methods). The ESM results are derived from CMIP6 under the "historical" (1948-2014) and "SSP2-RCP4.5" (2015-2100) scenarios. The anomalies are computed by subtracting the climatological mean of 1961-1990. The shaded areas represent the 95% confidence intervals of CMIP6 ESMs. Slope and statistical significance of the linear trend is shown for each metric, with symbols "***", "**", "*" and "n.s." denoting "$p < 0.01$", "$p < 0.05$", "$p < 0.1$", "$p > 0.1$", respectively.

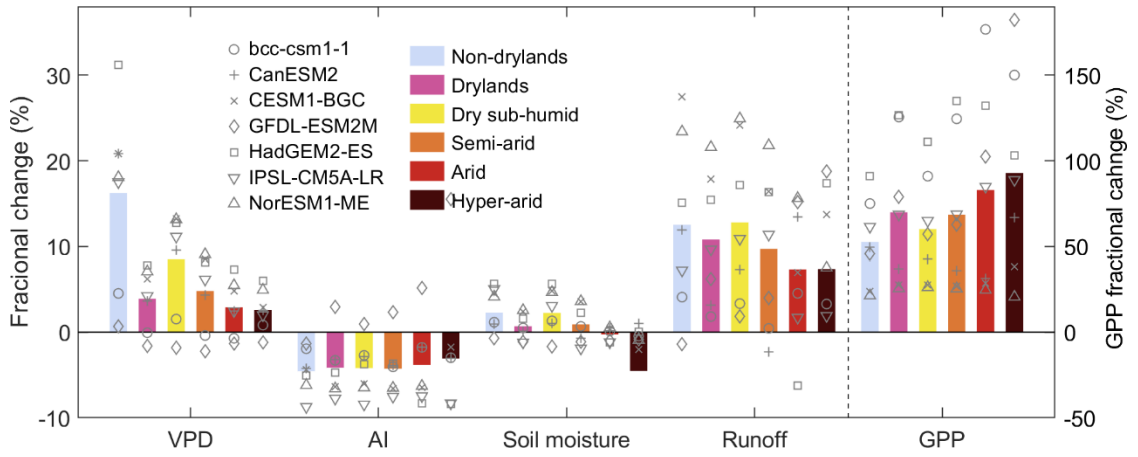

Supplementary Figure 6 | CO_2 physiological effects on surface aridity changes over global drylands. Bars (multi-model ensemble means) and symbols (individual models) show fractional changes in the five aridity metrics (VPD, AI, soil moisture, runoff and GPP) caused by plant physiological responses to a quadrupling of atmospheric CO_2, as averaged over AI-defined non-dryland, dryland and its four subcategories. These fractional changes are calculated by subtracting values of the first 20 years of the CMIP5 "esmFixClim1" runs (see Supplementary Methods) from that of the last 20 years. Note that GPP uses, exclusively, the scale on the right of the plot.

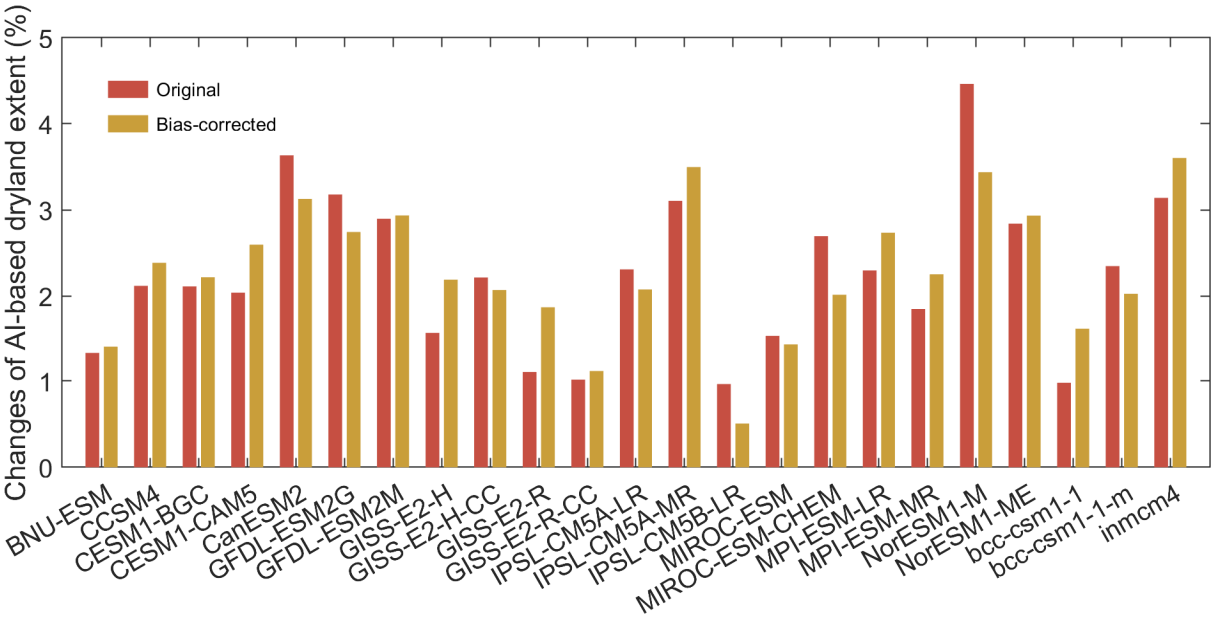

Supplementary Figure 7 | Future changes of AI-estimated global dryland extent (%) based on original versus bias-corrected CMIP5 ESM projections (under RCP4.5). The changes are calculated as the differences in AI-based dryland extent between 2090s and the baseline period of 1961-1990.

References

1 Harris, I., Jones, P. D., Osborn, T. J. & Lister, D. H. Updated high-resolution grids of monthly climatic observations — the CRU TS3.10 Dataset. *Int. J. Climatol.* **34**, 623-642 (2014).

2 Chen, M., Xie, P., Janowiak, J. E. & Arkin, P. A. Global land precipitation: A 50-yr monthly analysis based on gauge observations. *J. Hydrometeorol.* **3**, 249-266 (2002).

3 Matsuura, K. & Willmott, C. J. Terrestrial precipitation: 1900-2008 gridded monthly time series, Version 2.01. http://climate.geog.udel.edu/~climate/ (2010).

4 Huffman, G. J., Adler, R. F., Bolvin, D. T. & Gu, G. Improving the global precipitation record: GPCP Version 2.1. *Geophys. Res. Lett.* **36** (2009).

5 Schneider, U. *et al.* GPCC full data reanalysis version 6.0 at 1.0°: monthly land-surface precipitation from rain-gauges built on GTS-based and historic data. https://doi.org/10.5676/DWD_GPCC/FD_M_V7_100 (2011).

6 Beck, H. E. *et al.* MSWEP: 3-hourly 0.25 global gridded precipitation (1979-2015) by merging gauge, satellite, and reanalysis data. *Hydrol. Earth Syst. Sci.* **21**, 589-615 (2017).

7 Rodell, M. *et al.* The Global Land Data Assimilation System. *Bull. Am. Meteorol. Soc.* **85**, 381-394 (2004).

8 Kistler, R. *et al.* The NCEP–NCAR 50-year reanalysis: monthly means CD-ROM and documentation. *Bull. Am. Meteorol. Soc.* **82**, 247-268 (2001).

9 Sheffield, J., Goteti, G. & Wood, E. F. Development of a 50-year high-resolution global dataset of meteorological forcings for land surface modeling. *J. Clim.* **19**, 3088-3111 (2006).

10 Rienecker, M. M. *et al.* MERRA: NASA's Modern-Era Retrospective Analysis for Research and Applications. *J. Clim.* **24**, 3624-3648 (2011).

11 Dee, D. P. *et al.* The ERA-Interim reanalysis: configuration and performance of the data assimilation system. *Q. J. Roy. Meteor. Soc.* **137**, 553-597 (2011).

12 Hoffmann, L. *et al.* From ERA-Interim to ERA5: the considerable impact of ECMWF's next-generation reanalysis on Lagrangian transport simulations. *Atmos. Chem. Phys.* **19**, 3097-3124 (2019).

13 Martens, B. *et al.* GLEAM v3: Satellite-based land evaporation and root-zone soil moisture. *Geosci. Model Dev.* **10**, 1903-1925 (2017).

14 Abatzoglou, J. T., Dobrowski, S. Z., Parks, S. A. & Hegewisch, K. C. TerraClimate, a

high-resolution global dataset of monthly climate and climatic water balance from 1958-2015. *Sci. Data* **5**, 170191 (2018).

15 Berg, A., Sheffield, J. & Milly, P. C. D. Divergent surface and total soil moisture projections under global warming. *Geophys. Res. Lett.* **44**, 236-244 (2017).

16 Dai, A., Qian, T., Trenberth, K. E. & Milliman, J. D. Changes in continental freshwater discharge from 1948 to 2004. *J. Clim.* **22**, 2773-2792 (2009).

17 Dai, A. & Trenberth, K. E. Estimates of freshwater discharge from continents: latitudinal and seasonal variations. *J. Hydrometeorol.* **3**, 660-687 (2002).

18 Hobeichi, S., Abramowitz, G., Evans, J. & Beck, H. E. Linear Optimal Runoff Aggregate (LORA): a global gridded synthesis runoff product. *Hydrol. Earth Syst. Sci.* **23**, 851-870 (2019).

19 Tucker, C. J. *et al.* An extended AVHRR 8-km NDVI dataset compatible with MODIS and SPOT vegetation NDVI data. *Int. J. Remote Sens.* **26**, 4485-4498 (2005).

20 Pinzon, J. & Tucker, C. A non-stationary 1981–2012 AVHRR NDVI3g time series. *Remote Sens.* **6**, 6929-6960 (2014).

21 Zhu, Z. *et al.* Greening of the Earth and its drivers. *Nat. Clim. Change* **6**, 791-795 (2016).

22 Taylor, K. E., Stouffer, R. J. & Meehl, G. A. An overview of CMIP5 and the experiment design. *Bull. Am. Meteorol. Soc.* **93**, 485-498 (2012).

23 Eyring, V. *et al.* Overview of the Coupled Model Intercomparison Project Phase 6 (CMIP6) experimental design and organization. *Geosci. Model Dev.* **9**, 1937-1958 (2016).

24 Betts, R. A. & McNeall, D. How much CO_2 at 1.5 °C and 2 °C? *Nat. Clim. Change* **8**, 546-548 (2018).

25 Zhang, W., Zhou, T., Zou, L., Zhang, L. & Chen, X. Reduced exposure to extreme precipitation from 0.5 degrees C less warming in global land monsoon regions. *Nat. Commun.* **9**, 3153 (2018).

26 Feng, S. & Fu, Q. Expansion of global drylands under a warming climate. *Atmos. Chem. Phys. Discuss.* **13**, 14637-14665 (2013).

27 Sitch, S. *et al.* Trends and drivers of regional sources and sinks of carbon dioxide over the past two decades. *Biogeosciences Discuss.* **10**, 20113-20177 (2013).

28 Warszawski, L. *et al.* The Inter-Sectoral Impact Model Intercomparison Project (ISI–MIP): project framework. *Proc. Natl. Acad. Sci. USA* **111**, 3228-3232 (2014).

29 Zhou, S. *et al.* Land-atmosphere feedbacks exacerbate concurrent soil drought and atmospheric aridity. *Proc. Natl. Acad. Sci. USA* **116**, 18848-18853 (2019).

30 Huang, J., Yu, H., Guan, X., Wang, G. & Guo, R. Accelerated dryland expansion under climate change. *Nat. Clim. Change* **6**, 166-171 (2016).

31 Li, Y., Chen, Y. & Li, Z. Dry/wet pattern changes in global dryland areas over the past six decades. *Glob. Planet. Change* **178**, 184-192 (2019).

32 Fu, Q. & Feng, S. Responses of terrestrial aridity to global warming. *J. Geophys. Res. Atmos.* **119**, 7863-7875 (2014).

33 Park, C.-E. *et al.* Keeping global warming within 1.5 °C constrains emergence of aridification. *Nat. Clim. Change* **8**, 70-74 (2018).

34 Scheff, J. & Frierson, D. M. W. Terrestrial aridity and its response to greenhouse warming across CMIP5 climate models. *J. Clim.* **28**, 5583-5600 (2015).

35 Koutroulis, A. G. Dryland changes under different levels of global warming. *Sci. Total Environ.* **655**, 482-511 (2019).

36 Asadi Zarch, M. A., Sivakumar, B., Malekinezhad, H. & Sharma, A. Future aridity under conditions of global climate change. *J. Hydrol.* **554**, 451-469 (2017).

37 Greve, P. *et al.* Global assessment of trends in wetting and drying over land. *Nat. Geosci.* **7**, 716-721 (2014).

38 Greve, P. & Seneviratne, S. I. Assessment of future changes in water availability and aridity. *Geophys. Res. Lett.* **42**, 5493-5499 (2015).

39 Ukkola, A. M. *et al.* Reduced streamflow in water-stressed climates consistent with CO_2 effects on vegetation. *Nat. Clim. Change* **6**, 75-78 (2015).

40 Lu, X., Wang, L. & McCabe, M. F. Elevated CO_2 as a driver of global dryland greening. *Sci. Rep.* **6**, 20716 (2016).

41 Wang, J. *et al.* Recent global decline in endorheic basin water storages. *Nat. Geosci.* **11**, 926-932 (2018).

42 Morgan, J. A. *et al.* C4 grasses prosper as carbon dioxide eliminates desiccation in warmed semi-arid grassland. *Nature* **476**, 202-205 (2011).

43 Fensholt, R. *et al.* Greenness in semi-arid areas across the globe 1981–2007 — an Earth Observing Satellite based analysis of trends and drivers. *Remote Sens. Environ.* **121**, 144-158 (2012).

44 Donohue, R. J., Roderick, M. L., McVicar, T. R. & Farquhar, G. D. Impact of CO_2 fertilization on maximum foliage cover across the globe's warm, arid environments. *Geophys. Res. Lett.* **40**, 3031-3035 (2013).

45 Brandt, M. *et al.* Satellite passive microwaves reveal recent climate-induced carbon losses

in African drylands. *Nat. Ecol. Evol.* **2**, 827-835 (2018).

46 Andela, N., Liu, Y. Y., van Dijk, A. I. J. M., de Jeu, R. A. M. & McVicar, T. R. Global changes in dryland vegetation dynamics (1988-2008) assessed by satellite remote sensing: comparing a new passive microwave vegetation density record with reflective greenness data. *Biogeosciences* **10**, 6657-6676 (2013).